

Ultrasonic phased array phase shift migration imaging of irregular surface components using attenuation compensation and anti-aliasing technique



Juncen Wu ^{a,b}, Hongwei Hu ^{a,b,*}, Yongfeng Song ^c, Duo Lyu ^{a,b}, Xiongbing Li ^c

^a College of Automotive and Mechanical Engineering, Changsha University of Science and Technology, Changsha, 410114, China

^b Hunan Province University Key Laboratory of Intelligent Testing and Control Technology for Engineering Equipment, Changsha, 410114, China

^c School of Traffic and Transportation Engineering, Central South University, Changsha, 410075, China

ARTICLE INFO

Keywords:

Ultrasonic phased-array imaging
Irregular surface components
Attenuation compensation
Anti-aliasing technique

ABSTRACT

Extended non-stationary phase shift migration (ENPSM) is a promising imaging algorithm for ultrasonic phased array testing of components with irregular surfaces. In this paper, ENPSM is developed further by combining attenuation compensation (AC) with an anti-aliasing (AA) technique, in an approach called AC-AA-ENPSM, to address the negative effects of attenuation during ultrasonic wave propagation in metals and of jagged medium interface determined by traditional rectangular window. The attenuation term in AC-AA-ENPSM is measured by immersion testing with referenced samples. An anti-aliasing technique is used to smooth the spatial velocity distribution based on the weights of different velocities on a pixel grid. Experiments are performed on objects with irregular surfaces, varying attenuation characteristics and side-drilled hole (SDH) defects. A comparison of the results shows that the proposed AC-AA-ENPSM algorithm has the advantage of a higher signal-to-noise ratio (SNR) than traditional ENPSM. Moreover, the proposed algorithm has a computational efficiency at least 40 times higher than the total Focusing Method (TFM) algorithm, and the SNR difference of them is less than 2 dB.

1. Introduction

In the field of non-destructive testing (NDT), ultrasonic imaging with the phase shift migration (PSM) method [1] has drawn attention and has been widely used for various types of detection objects. PSM originated in the domain of geological imaging [2], and obtains accurate wavefield information through wavefield extrapolation based on wave equation, which allows the wave velocity to vary with depth. Unlike delay-and-sum methods such as the synthetic aperture focusing technique (SAFT) [3], PSM is calculated based on the fast Fourier transform (FFT) in the wavenumber-frequency domain, meaning that it has higher computational efficiency.

Initially, PSM was applied only to single-transducer ultrasonic testing [4,5] under the conditions of an exploding reflector, in which the scatter was considered as an exploding source in the physical medium with half the velocity of ultrasound. Then, Skjelvareid et al. [5] combined PSM with the omega-k algorithm to create a new method of performing multi-layer imaging with more efficiency for stacked objects, called the multi-layer omega-k (MULOK) algorithm. Qin et al. [6] presented the generalized phase shift migration (GPSM) algorithm to deal with irregularly layered objects using immersed testing. Lukomski et al.

[7] proposed the non-stationary phase shift method (NSPSM) for imaging layered objects, in which the surface is not perpendicular to the axis of the transducer and the layers are not horizontal. To avoid discontinuities in the frequency domain, the window of the NSPSM is carried out in the spatial domain not in the wavenumber domain. Mao et al. [8] proposed a fast interface reconstruction method based on virtual points measuring to combine with the NSPSM. However, since ultrasonic phased arrays are widely used in NDT, the single-transducer-based PSM methods described above need to be adapted to ultrasonic phased array testing.

Thus, PSM was revised for use with full matrix capture (FMC) data of ultrasonic phased arrays for stacked objects [9], in an approach known as the extended phase shift migration (EPSM) method. Furthermore, PSM with ultrasonic phased array was developed to cope with complex detection conditions, such as objects with irregular surfaces [10,11], unknown ultrasonic velocities [12], and medical imaging with anisotropy [13]. Of these, extended non-stationary phase shift migration (ENPSM) [11] is a promising method that was designed for immersed or finitely stacked objects that are inhomogeneous in both the depthwise and the lateral directions. It is based on EPSM with non-stationary convolution filter theory.

* College of Automotive and Mechanical Engineering, Changsha University of Science and Technology, Changsha, 410114, China
E-mail address: hhwlucky@163.com (H. Hu).

Nevertheless, when ENPSM is applied to a highly attenuative material such as copper, the imaging results have poor resolution for deep defects, and they exhibit baffling artifacts. Recently, Jin et al. [14] proposed a PSM method with ultrasonic attenuation compensation, in which the ultrasonic attenuation coefficient of samples was measured and compensated in different materials by a single transducer. This method was experimentally shown to greatly improve the imaging results in terms of high resolution and low time cost. However, we note that this was a single-transducer-only application, and these researchers focused on polymer composites with absorption attenuation and strong dispersion. This approach needs to be extended to accommodate ultrasonic phased arrays and metallic test objects. Here, the method of measuring attenuation is used for compensation according to [15,16], as the attenuation of metals is a unique property that varies by type.

In addition, immersive PSM imaging of irregular surface components requires prior knowledge of the velocity distribution in the region of interest, due to the inhomogeneity of the depth and lateral directions. Qin et al. [6] defined the velocity distribution on a discrete grid as a Bernoulli distribution, and a rectangular window function was used for filtering in the frequency domain during migration processing. Lukomski et al. [17] attempted to introduce a rounded rectangular window function to eliminate the negative effects of sudden, sharp shifts in the velocity distribution. But this study did not consider smoothing of the spatial window based on the true velocity distribution by calculating a more accurate proportion of the different medium velocities on a discrete grid. Also, the operation of smooth slows down their computation process. We note that this smoothing method is very similar to the anti-aliasing technique in image processing, in which the mesh density is increased and sub-grids are merged within the original mesh to take the mean value, thus eliminating the strong jaggedness of the image boundaries.

In this paper, we therefore introduce an improved attenuation compensation term for metals and an anti-aliasing technique, to form an enhanced version of ENPSM. The attenuation coefficients of the experimental samples are measured to enable matching and admixing of layers with different velocities. To compare and analyze the effects of attenuation compensation (AC-ENPSM), anti-aliasing (AA-ENPSM), and both (AC-AA-ENPSM) on phased array imaging, a series of immersive ultrasonic experiments will be conducted. The benefits of frequency domain processing and bandwidth selection for enhanced ENPSM are also discussed. Finally, the proposed method is compared to the total focusing method (TFM) algorithm, a well-established technique for ultrasonic phased array imaging.

2. Method

2.1. ENPSM algorithm

We assume that when the center frequency of the transducer in ultrasonic NDT is low (e.g., 2.5 or 5 MHz), the dispersion of the phase velocity for bulk waves in metals is negligible. The sound pressure at a given moment and location $p(x, z, t)$ in the two-dimensional plane xOz satisfies the wave equation [18]:

$$\left(\frac{\partial^2}{\partial x^2} + \frac{\partial^2}{\partial z^2} - \frac{1}{c^2} \frac{\partial^2}{\partial t^2} \right) p(x, z, t) = 0, \quad (1)$$

where c is the velocity of the ultrasonic wave in the medium; and t is the propagation time of the ultrasonic wave. From a Fourier transform of x , in Eq. (1), we have:

$$\left(\frac{\partial^2}{\partial z^2} + \frac{\omega^2}{c^2} - k_x^2 \right) P(k_x, z, \omega) = 0, \quad (2)$$

and a general form of Eq. (2) is obtained as:

$$P(k_x, z, \omega) = P_U(k_x, z=0, \omega) \exp(jk_z z) + P_D(k_x, z=0, \omega) \exp(-jk_z z), \quad (3)$$

$$k_z = \text{sgn}(\omega) \sqrt{\frac{\omega^2}{c^2} - k_x^2}, \quad \frac{\omega^2}{c^2} \geq k_x^2, \quad (4)$$

where ω is the angular frequency; k_x is the wavenumber in the x -direction; k_z is the wavenumber in the z -direction; P_U and P_D represent the pressures in the upward and downward wave propagation directions, respectively; and $\exp(\pm jk_z z)$ is known as the phased migration factor (PMF). The positive and negative signs in the PMF are chosen based on the boundary constraints: when the ultrasonic wave propagates in the positive direction of the z -axis, the negative sign is used; otherwise, the positive sign is used. Hence, when the scatterer is the source of propagation, we have:

$$P_r(k_x, z, \omega) = P_r(k_x, z=0, \omega) \Psi(k_x, z, \omega). \quad (5)$$

Here, we name PMF as $\Psi(k_x, z, \omega)$, with $\Psi(k_x, z, \omega) = \exp(jk_z z)$. The PMF is different for various velocity. When performing an immersed test of irregular surface components, the velocities of the water and the test object are distributed unevenly over the whole region. The water layer and test object are then sliced into equal sub-layers of thickness Δz in the z -direction, and each sub-layer is further divided into grids in the x -direction. We assume that there are two materials in the x -direction and that the velocity distributions of materials 1 and 2 are $\Omega_1(x, z)$ and $\Omega_2(x, z)$, respectively. This process can be viewed as a physical filter in the frequency-space domain when waves are incident from irregular surfaces. For materials 1 and 2, the velocity distributions are given [10,11] by Eq. (6):

$$\Omega_{1,2}(x, z) = \begin{cases} 1, & c(x, z) = c_{1,2}, \\ 0, & \text{otherwise} \end{cases} \quad (6)$$

Where c_1 and c_2 are the velocity of longitudinal wave in materials 1 and 2. The transmitting and receiving wavefields are then established depending on their respective velocities for image reconstruction. Taking the i th emission of the element as an example, the frequency domain of the received wavefield can be represented as $P_{ri}(x, z, \omega|i)$, and the frequency domain of the transmitted wavefield as $P_{ti}(x, z, \omega|i)$, for material 1. Similarly, the frequency domain of the received wavefield can be represented as $P_{r2}(x, z, \omega|i)$, and the frequency domain of the transmitted wavefield as $P_{t2}(x, z, \omega|i)$, for material 2.

The wavefields are extrapolated and admixed in the space $z > 0$ (see Fig. 1), as follows [10]:

$$P(x, z + \Delta z, \omega|i) = P_r(x, z + \Delta z, \omega|i) P_t^*(x, z + \Delta z, \omega|i), \quad (7)$$

where

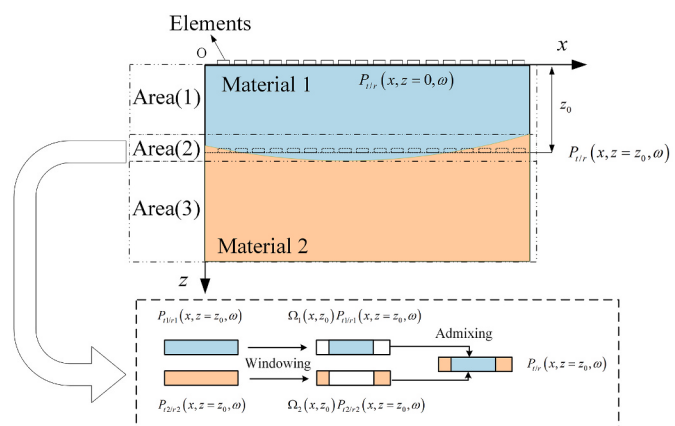


Fig. 1. Schematic diagram of immersed irregular surface components using an ultrasonic phased array.

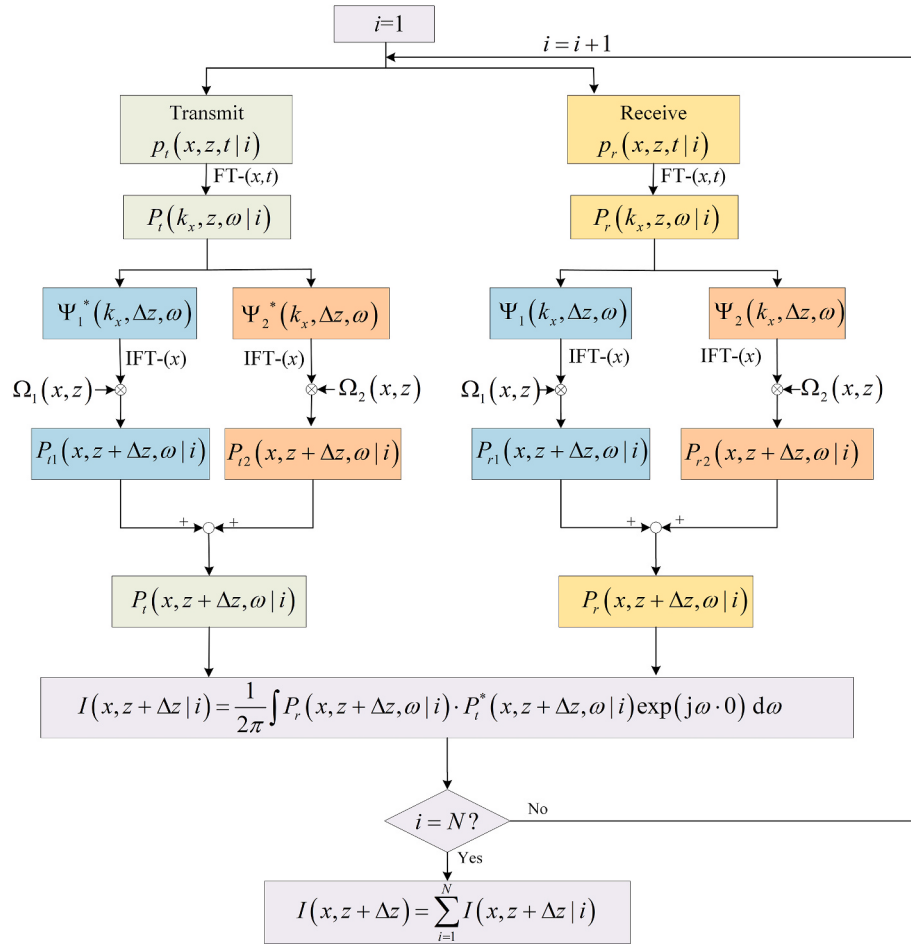


Fig. 2. Workflow for the ENPSM method with extrapolation and admixing in each sub-layer.

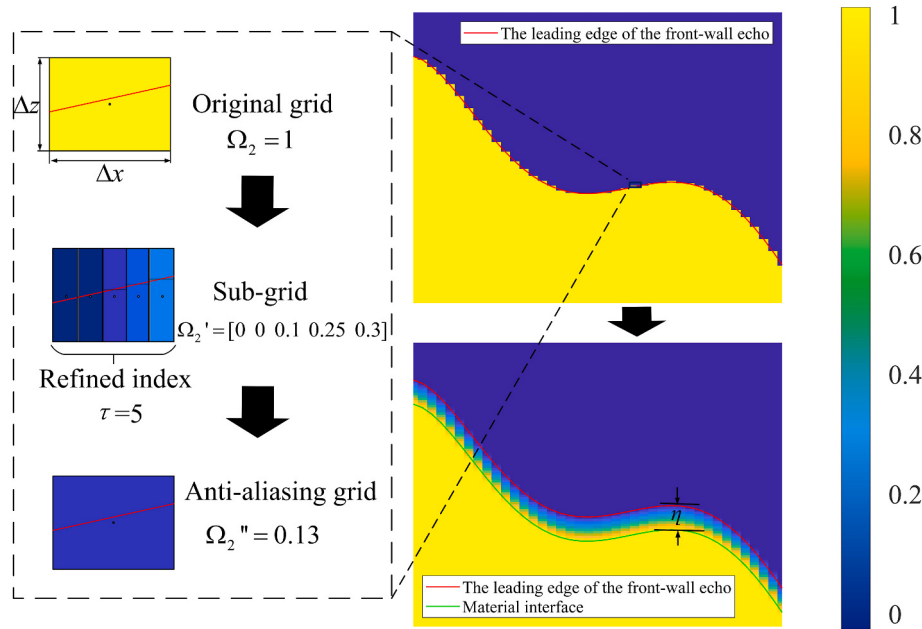


Fig. 3. Schematic diagram of the anti-aliasing window. The color mapping depicts the occupation weights for material 2. (For interpretation of the references to color in this figure legend, the reader is referred to the Web version of this article.)

$$P_t(x, z + \Delta z, \omega | i) = \Omega_1(x, z + \Delta z) IFT_{k_x \rightarrow x} \left\{ \Psi_1^*(k_x, \Delta z, \omega) FT_{x \rightarrow k_x} [P_t(x, z, \omega | i)] \right\} + \Omega_2(x, z + \Delta z) IFT_{k_x \rightarrow x} \left\{ \Psi_2^*(k_x, \Delta z, \omega) FT_{x \rightarrow k_x} [P_t(x, z, \omega | i)] \right\}, \quad (8)$$

$$P_r(x, z + \Delta z, \omega | i) = \Omega_1(x, z + \Delta z) IFT_{k_x \rightarrow x} \left\{ \Psi_1(k_x, \Delta z, \omega) FT_{x \rightarrow k_x} [P_r(x, z, \omega | i)] \right\} + \Omega_2(x, z + \Delta z) IFT_{k_x \rightarrow x} \left\{ \Psi_2(k_x, \Delta z, \omega) FT_{x \rightarrow k_x} [P_r(x, z, \omega | i)] \right\}. \quad (9)$$

It should be noted that the procedure is performed layer-by-layer with discrete z-direction sub-layers. The condition for reconstructing the image is $t = 0$ [19], and hence we have:

$$I(x, z | i) = p(x, z, t = 0 | i) = \frac{1}{2\pi} \int P(x, z, \omega | i) \exp(j\omega \cdot 0) d\omega. \quad (10)$$

Finally, all the emitted elements are superimposed to obtain the imaging results $I(x, z)$:

$$I(x, z) = \sum_{i=1}^N I(x, z | i). \quad (11)$$

To illustrate the principle of the original ENPSM, the workflow is shown in Fig. 2. The improved PMF and the $\Omega_{1,2}(x, z)$ are described in Sections 2.2 and 2.3, respectively. It is crucial to select a certain frequency range $[\omega_{\min}, \omega_{\max}]$ for computing the ENPSM algorithm. The frequency range should be selected around the transducer's center frequency, and the bandwidth selection may have an impact on the time cost.

2.2. Ultrasonic attenuation measurement and compensation

As shown in [14,20], the attenuation amplitude and propagation distance r follow a frequency power law when an acoustic wave propagates in a medium:

$$A = A_0 \exp(-jk(\omega)r). \quad (12)$$

In Ref. [15], one type of wavenumber $k_{ref}(\omega)$ was given as:

$$k_{ref}(\omega) = \omega / c + ja|\omega|^n + a\omega|\omega|^{n-1} \tan(\pi n / 2), \quad (13)$$

where the term $ja|\omega|^n$ is the acoustic attenuation, and the term $a\omega|\omega|^{n-1} \tan(\pi n / 2)$ represents the dispersion effects. This operation applies to a viscoelastic material with absorption attenuation and strong dispersion, such as biological tissues or polymer. However, most types of metal don't have strong viscoelastic properties, which means that very little energy is lost when mechanical energy is turned into thermal energy during ultrasonic propagation. Hence, the wavenumber term can be expressed as [18]:

$$k(\omega) = \omega / c + ja(\omega), \quad (14)$$

where $a(\omega)$ is the measured attenuation coefficient of ultrasound traveling through a single medium. It consists of the attenuation due to grain scattering and weak absorption in elastic solids; and its measuring method will be discussed later. In an immersive ultrasonic inspection system with a single transducer, a simplified model of the measured u th back-wall signal can be written as [21]:

$$S_{B,u}(\omega) = S_0(\omega) \cdot T_{ws} \cdot R_{ss}^{2u-1} \cdot T_{sw} \cdot D_{B,u} \cdot A_{B,u}. \quad (15)$$

with

$$R_{ss} = (\rho_s c_s - \rho_w c_w) / (\rho_s c_s + \rho_w c_w),$$

$$D_{B,u} = 1 - \exp(-2\pi js)[J_0(2\pi / s) + j J_1(2\pi / s)],$$

$$s = (2z_0 c_w + 2udc_s) / (\omega_0 r_0^2),$$

$$A_{B,u} = \exp(-2\alpha_w(\omega)z_0 - 4\alpha(\omega)ud),$$

where $S_0(\omega)$ is the spectrum of the transmitted signal; T_{ws} and T_{sw} are the

transmission coefficients of the water-solid interface and the solid-water interface, respectively; R_{ss} is the reflection coefficient of the solid-solid interface; $D_{B,u}$ is the diffraction correction coefficient of the u th back-wall signal; $A_{B,u}$ is the attenuation term of the u th back-wall echo signal, including the attenuation of sound propagation in water and in solids; ρ is the material density (where the subscript s represents the sample, and w represents water); J_0 and J_1 are Bessel functions; z_0 is the distance between the transducer and the front wall of the sample; d is the thickness of the sample; ω_0 is the center frequency of the ultrasound wave; r_0 is the radius of the transducer; and the attenuation coefficient of water $\alpha_w(\omega)$ is determined as set out in Ref. [22].

By dividing the measured the u th back-wall echo signal by the v th back-wall echo signal, we obtain

$$\frac{S_{B,u}(\omega)}{S_{B,v}(\omega)} = \frac{S_0(\omega) \cdot T_{ws} \cdot R_{ss}^{2u-1} \cdot T_{sw} \cdot D_{B,u} \cdot A_{B,u}}{S_0(\omega) \cdot T_{ws} \cdot R_{ss}^{2v-1} \cdot T_{sw} \cdot D_{B,v} \cdot A_{B,v}}, \quad (16)$$

and then

$$\alpha(\omega) = -\frac{1}{2(u-v)d} \ln \left(\left| \frac{1}{R_{ss}^{2(u-v)}} \frac{D_{B,v}}{D_{B,u}} \frac{S_{B,u}(\omega)}{S_{B,v}(\omega)} \right| \right). \quad (17)$$

After obtaining the attenuation coefficient according to the power law of scattering attenuation, we can express the attenuation compensation as follows:

$$P(\omega, z + \Delta z) = P(\omega, z) \exp(\alpha(\omega) \cdot \Delta z). \quad (18)$$

combining Eqs. (5) and (18), we get the PMFs with attenuation compensation in each layer in the z -direction:

$$\Phi_{1,2}(k_x, \Delta z, \omega) = \Psi_{1,2}(k_x, \Delta z, \omega) \cdot \exp(\alpha_{1,2}(\omega) \cdot \Delta z), \quad (19)$$

where $\alpha(\omega)$ is the attenuation of the material; $*$ is a complex conjugate; subscript 1 represents material 1; and subscript 2 represents material 2. For application, it could be replaced $\Psi_{1,2}(k_x, z, \omega)$ with $\Phi_{1,2}(k_x, \Delta z, \omega)$ in Eqs. (8) and (9). Because calculating diffraction loss using the beam model is beyond the scope of this paper, the compensation process at a very deep position may be excessive for some strongly attenuative material. Therefore, a certain depth value can be chosen to truncate the attenuation compensation thus maintaining the same amount of compensation at subsequent depths.

2.3. Anti-aliasing technique

As shown in Eq. (6), a rectangular window function was used as a filter to process the different velocities of the detection region. However, the lateral resolution is limited as in the original ENPSM, and cannot be further refined, resulting in a rough and jagged interface between two media and affecting the following imaging computation. The velocity distribution is set to 0 or 1 when a rectangular window function is employed to determine the weights of various materials in each pixel grid. Hence, we focus on further refining the pixel grid near the material interface to get a relatively accurate velocity distribution.

It should be noted that the lateral size of the pixel grid is restricted to the pitch of the ultrasonic phased array, so the lateral grid is the main focus of the anti-aliasing procedure. Firstly, as shown in Fig. 3, the red line (as established in Sec. 4.1) indicates the leading edge of the front-wall echo. The green line is an offset of the leading edge representing the material interface, where the offset distance is denoted by η . Thus, the space between the red and green lines generates an anti-aliasing region. The center of each grid is used as a simplified description of its

location. Originally, if the center of the grid is at or below the red line, it is material 2; otherwise, it is material 1 [10]. However, to avoid jaggedness, we then divide each grid into τ smaller sub-grids in the x -direction, called the τ refined index. The window function of a sub-grid is calculated according to the following equation:

$$\Omega'_2 = \begin{cases} [g(x_{\text{sub-g}}) - z_{\text{sub-g}}] / \eta & , 0 \leq g(x_{\text{sub-g}}) - z_{\text{sub-g}} \leq \eta, \\ 0 & , \text{otherwise} \end{cases}, \quad (20)$$

where $(x_{\text{sub-g}}, z_{\text{sub-g}})$ is the sub-grid center; $g(x)$ is the geometric contour curve of leading edge. Actually, this is a linear transition from zero to one within the anti-aliasing region. To maintain the horizontal dimension of the pixel grid after imaging, the window function of internal sub-grids is averaged for each grid:

$$\Omega''_2 = \frac{1}{\tau} \sum \Omega'_2(x_{\text{sub-g}}, z_{\text{sub-g}}), \quad (21)$$

where Ω''_2 represents the anti-aliasing window function relative to the second layer of the medium. The larger the value of τ is, the smaller the sub-grid is. Finally, the anti-aliasing window function relative to the first layer of the medium Ω''_1 is:

$$\Omega''_1 = |1 - \Omega''_2|. \quad (22)$$

In this way, the anti-aliasing velocity distribution window function is obtained. In Sec. 4.1, we will compare the effects of anti-aliasing on the ENPSM imaging results and investigate various values for τ and η .

2.4. AC-AA-ENPSM algorithm

The AC-AA-ENPSM algorithm is computed by first using the anti-aliasing technique, and then executing the AC-ENPSM algorithm. Pseudocode for our method is shown in Algorithm 1. Prior to PSM imaging, the weights of two media are determined in terms of irregular surface, with anti-aliasing process provided in the last section. Let the imaging area in the z -direction be $z \in [z_{\min}, z_{\max}]$, and the maximum and minimum peak values of the geometric contour curve $g(x)$ are g_{\max} and g_{\min} , respectively. Then, we can then divide the imaging area into three parts, as follows:

Area (1): This is the area from z_{\min} to g_{\min} , where the velocity $c = c_1$ is a constant. Due to the fact that the depth sequence of sub-layers in this area has independent and identical PMF, the imaging algorithm may be computed concurrently, allowing for a simple computation to improve computation speed.

Area (2): This is the region from g_{\min} to g_{\max} . Since the applied surface is irregular, the velocity distribution between c_1 and c_2 is totally arbitrary. A layer-by-layer iterative implementation must be used to compute the PMF throughout the imaging process, where the attenuation compensation stipulated in Sec 2.2 will also be executed in these iterations.

Area (3): This is the area from g_{\max} to z_{\max} , where the velocity $c = c_2$ is also a constant. A strategy similar to that of Area (1) will be implemented. Finally, the AC-AA-ENPSM imaging result can be output.

Algorithm 1. AC-AA-ENPSM

Input: Full matrix data $S(i, q, t)$ (transmitted by i^{th} element and received by q^{th} element); frequency range $[\omega_{\min}, \omega_{\max}]$; velocities c_1 and c_2 ; PMF with attenuation compensation $\Phi_1(k_x, z, \omega)$ and $\Phi_2(k_x, z, \omega)$; imaging parameters $x, z, \Delta x$, and Δz ; offset distance η ; refined index τ .

- 1: Synthesize the B-scan image based on the full matrix data and normalize the magnitude, set the magnitude threshold to obtain the surface contour $g(x, z)$, extract the maximum g_{\max} and minimum g_{\min} of the contour, and divide the computational area into Area (1), Area (2), Area (3);
- 2: Replace the rectangular window function with an anti-aliasing window function

$$\Omega_1(x, z) \rightarrow \Omega_1''(x, z); \Omega_2(x, z) \rightarrow \Omega_2''(x, z);$$

3: **for** $i=1:64$ **do**

4: Generate P_t and P_r at $z=0$,

$$P_t(x, z=0, t | i) = \begin{cases} \delta(t) & x = x_i \\ 0 & \text{otherwise} \end{cases},$$

$P_r(x=x_q, z=0, t | i) = S(i, q, t)$, x_q represents the location of q^{th} element in the x -direction.

- 5: Imaging process with depth sequence $z \in [z_{\min}, g_{\min}]$ without using a window function, calculated based on c_1 , sound velocity of material 1, in the Area (1). After FFT process of x and t , imaging according to Eqs. (7) and (10) with

$$P_t(x, z, \omega | i) = \underset{k_x \rightarrow x}{IFT} [P_t(k_x, z=0, \omega | i) \Phi_1^*(k_x, z, \omega)],$$

$$P_r(x, z, \omega | i) = \underset{k_x \rightarrow x}{IFT} [P_r(k_x, z=0, \omega | i) \Phi_1(k_x, z, \omega)].$$

- 6: Start at $z = g_{\min}$ and end at $z = g_{\max}$ with a layer-by-layer iterative process in the Area (2). Run with

$$P_t(x, g_{\min} + \Delta z, \omega | i) = \Omega_1''(x, g_{\min} + \Delta z) \underset{k_x \rightarrow x}{IFT} \left\{ \Phi_1^*(k_x, \Delta z, \omega) \underset{x \rightarrow k_x}{FT} [P_t(x, g_{\min}, \omega | i)] \right\},$$

$$+ \Omega_2''(x, g_{\min} + \Delta z) \underset{k_x \rightarrow x}{IFT} \left\{ \Phi_2^*(k_x, \Delta z, \omega) \underset{x \rightarrow k_x}{FT} [P_t(x, g_{\min}, \omega | i)] \right\}$$

$$P_r(x, g_{\min} + \Delta z, \omega | i) = \Omega_1''(x, g_{\min} + \Delta z) \underset{k_x \rightarrow x}{IFT} \left\{ \Phi_1(k_x, \Delta z, \omega) \underset{x \rightarrow k_x}{FT} [P_r(x, g_{\min}, \omega | i)] \right\},$$

$$+ \Omega_2''(x, g_{\min} + \Delta z) \underset{k_x \rightarrow x}{IFT} \left\{ \Phi_2(k_x, \Delta z, \omega) \underset{x \rightarrow k_x}{FT} [P_r(x, g_{\min}, \omega | i)] \right\}$$

Imaging according to Eqs. (7) and (10). Note that this operation must be done layer by layer in Area (2);

- 7: Imaging process with depth sequence $z \in [g_{\max}, z_{\max}]$ without the application of a window function, calculated with velocity c_2 in the Area (3):

$$P_t(x, z, \omega | i) = \underset{k_x \rightarrow x}{IFT} [P_t(k_x, z = g_{\max}, \omega | i) \Phi_2^*(k_x, z - g_{\max}, \omega)],$$

$$P_r(x, z, \omega | i) = \underset{k_x \rightarrow x}{IFT} [P_r(k_x, z = g_{\max}, \omega | i) \Phi_1(k_x, z - g_{\max}, \omega)],$$

Imaging according to Eqs. (7) and (10).

8: **end for**

$$9: I(x, z) = \sum_{i=1}^N I(x, z | i);$$

10: Stitch Areas (1), (2), and (3) to get the complete image.

Output: Imaging result.

3. Experimental setup

3.1. Samples

As shown in Fig. 4(a and b), the experimental samples used in the experiments were an aluminum alloy with low attenuation characteristics and a copper alloy with high attenuation characteristics. The geometric contour curves for both samples were set to a sine curve with a period of 50 mm and an amplitude of 1 mm, i.e. $g_{spl}(x) = \sin(2\pi x/50)$. Each sample has six 1.5 mm diameter side-drilled hole (SDH) defects. For the copper alloy sample, the velocity of the longitudinal wave was 4,385.8 m/s and the density was 8,236.1 kg/m³. For the aluminum alloy sample, the velocity of the longitudinal wave was 6,353.9 m/s and the density was 2,728.7 kg/m³.

3.2. Measurement of ultrasonic attenuation

Attenuation measurements are carried out using a single transducer immersion test. The measurement equipment includes immersed plane transducers (OLYMPUS), a pulse transmitter and receiver JSC-DPR300 (Imaginant), a data acquisition card M4I.4420-X8 (Spectrum Instrumentation), motion control devices, and a computer, as shown in Fig. 4(d). An immersed plane transducer with center frequency 7.5 MHz and diameter 0.5 inch is used to measure the attenuation of the aluminum

alloy. Due to strong attenuation resulting in spectrum deviation, the attenuation of the copper alloy is measured by ones with center frequency 15 MHz and diameter 0.5 inch. Both signals are captured at a sampling frequency of 250 MHz. The top and bottom surfaces of each sample are parallel to the transducer surface, and there are no defects in the transducer detection area.

The velocity of the acoustic wave in water is 1,491.3 m/s. The first back-wall echo (BW1) and the second back-wall echo (BW2) of the A-scan signal are segmented. Their spectrum is then obtained by an FFT. The frequency domain information for BW1 and BW2 is introduced into Eq. (17) using the corresponding parameters of the measurement system, and the attenuation results for the samples are obtained as shown in Fig. 5. It should be noted that the attenuation coefficient of water is given by $\alpha_w = 2.53 \times 10^{-14}f^2$ [22].

3.3. Imaging experiment with ultrasonic phased array

As shown in Fig. 4(f), the imaging experiment setup consisted of a Vantage 64 LE research ultrasound system (Verasonics), a 64-array ultrasonic phased array transducer (Imasonic) with center frequency 5 MHz and pitch 0.5 mm, and a computer with 32G memory and Intel® Core™ i7-8700K CPU @ 3.70 GHz. All computational processing was done in MATLAB R2018b without the use of graphics processing unit (GPU) acceleration and parallel computation tool. Immersion testing

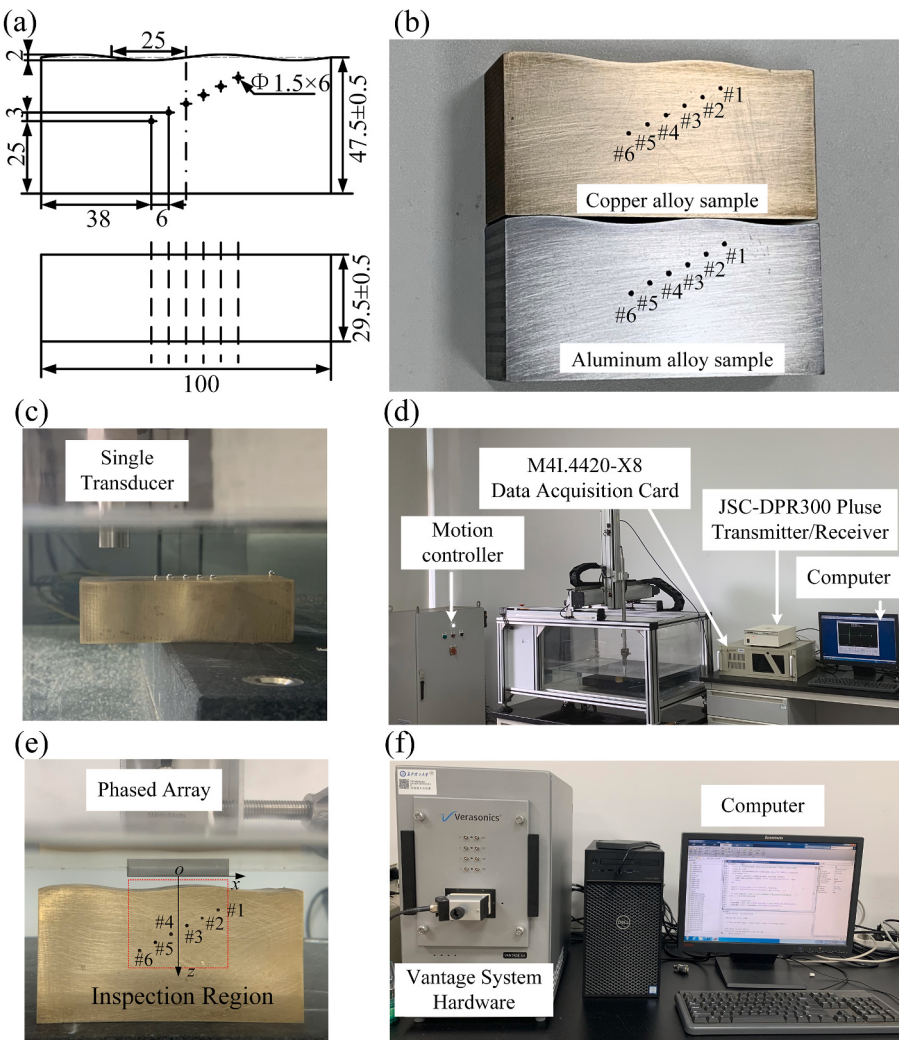


Fig. 4. Experimental setup for ultrasonic attenuation measurements and imaging experiments: (a, b) experimental samples; (c, d) equipment used for attenuation measurements; (e, f) equipment used for imaging experiments.

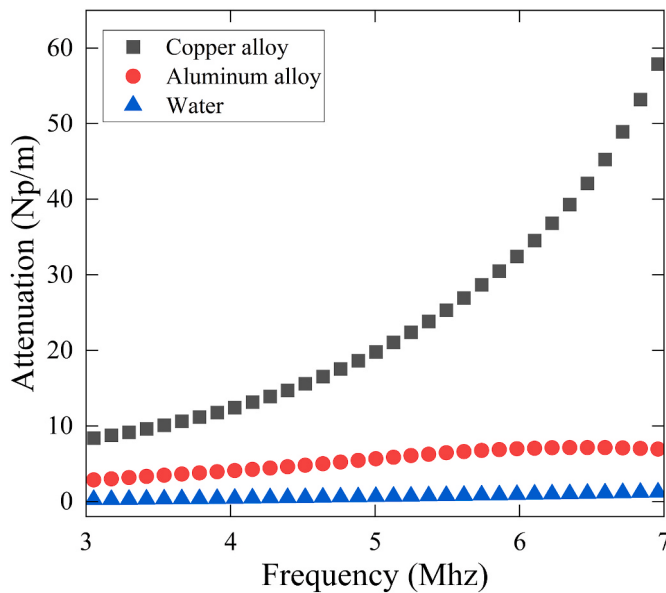


Fig. 5. Attenuation results for the experimental samples.

was performed on the aluminum alloy and copper alloy samples. The FMC data were collected at a sampling frequency of 50 MHz, and the size of the dataset was $1408 \times 64 \times 64$.

4. Results and discussion

4.1. AA-ENPSM without attenuation compensation

Initially, a synthetic B-scan is performed based on the FMC data to get the surface profile. The B-scan in Fig. 6(a) for extracting the geometric contour curve of the water-solid interface was performed using a phased array beamforming approach without a delay-law (focus on infinity) [23], where the received signals of neighboring M elements ($M = 9$ in our case) are superimposed directly and a synthetic larger aperture may be obtained. To detect the leading edge of the first front-wall

echoes, a threshold of -14dB is chosen for the beamforming B-scan image. Using a curve fitting technique, we can derive the geometric contour curve $g(x)$, as shown in Fig. 6(b). A fifth-order polynomial curve fits the data from -15.75 mm to 15.75 mm in the x -direction:

$$g(x) = -5.8397 \times 10^{-7}x^5 - 9.9114 \times 10^{-6}x^4 + 3.824 \times 10^{-4}x^3 + 5.2 \times 10^{-3}x^2 - 0.1254x + 2.586 .$$

The anti-aliasing experiments are performed with values for a refined index $\tau = 4$ and an offset distance $\eta = 0.10 \text{ mm}$ in Fig. 6(c); and the results for the copper alloy sample are shown in Fig. 6(d). When viewed from the perspective of the human eye, Fig. 6(d) has a boundary that is more natural and smoother than Fig. 6(b). As a consequence, the proposed method successfully achieves anti-aliasing on the velocity distribution map.

Through post-processing for the FMC data acquired by the Vantage 64 LE system, the imaging results of the ENPSM method, the anti-aliasing ENPSM (AA-ENPSM) imaging results with $\tau = 4$, and $\eta = 0.05, 0.10$ and 0.30 mm are shown in Fig. 7. The size of pixel grid is set as $0.1 \text{ mm} \times 0.5 \text{ mm}$ in Fig. 7. Because it is reasonable to assume that a higher refined index will lead to better imaging results, the refined index is fixed at $\tau = 4$ here to investigate the offset distance η in a univariate manner. The selected bandwidth is $4\text{--}6 \text{ MHz}$ for the copper alloy sample, and it will be discussed in Sec 4.2. Compared with ENPSM in Fig. 7(a), we can see that AA-ENPSM reduces the artifacts including the second front wall echo, and gives a smoother surface profile as shown in Fig. 7 (b-d). Increasing η improves the imaging with less noise for the copper alloy sample. Although increasing the offset distance η brings improvements by reducing the artifacts, it decreases the amplitude of the defects if η is set to an excessively large value, especially for the deepest one (SDH #6).

The effects of different values of τ and η on the anti-aliasing capability are then investigated in detail. To objectively measure the imaging quality of AA-ENPSM algorithm, the signal-to-noise ratio (SNR) is typically employed. It is calculated as [24]:

$$\text{SNR} = I_{\max} / \text{RMS}(I'), \quad (23)$$

where I_{\max} is the maximum amplitude (dB) of the defect area, and $\text{RMS}(I')$ is the root mean square of the defect-free background noise (dB). The green dotted area is the region of background noise for

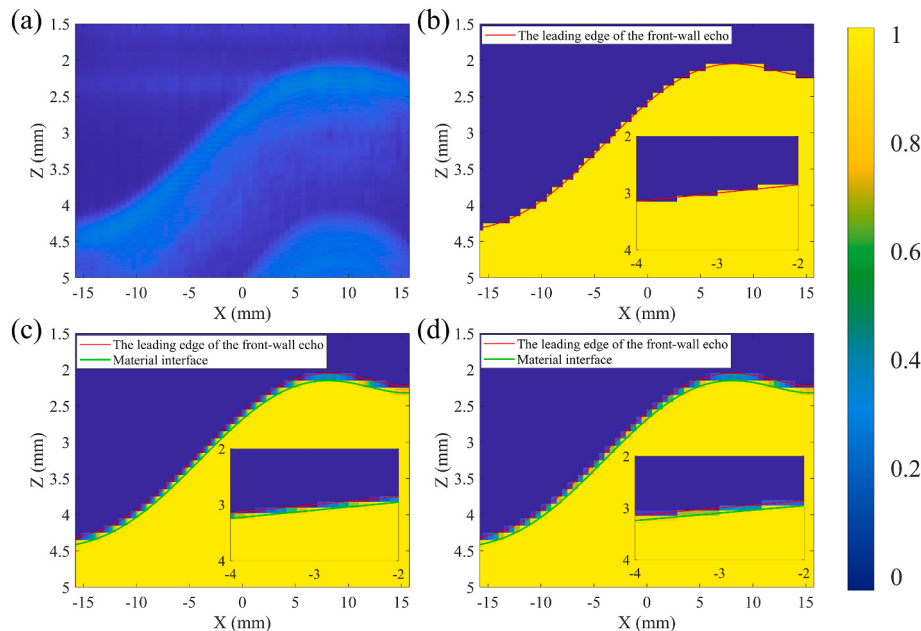


Fig. 6. Smoothing results from the anti-aliasing process: (a) synthetic B-scan; (b) rectangle window; (c) refined grid with offset distance $\eta = 0.10 \text{ mm}$ and refined index $\tau = 4$; (d) anti-aliasing results.

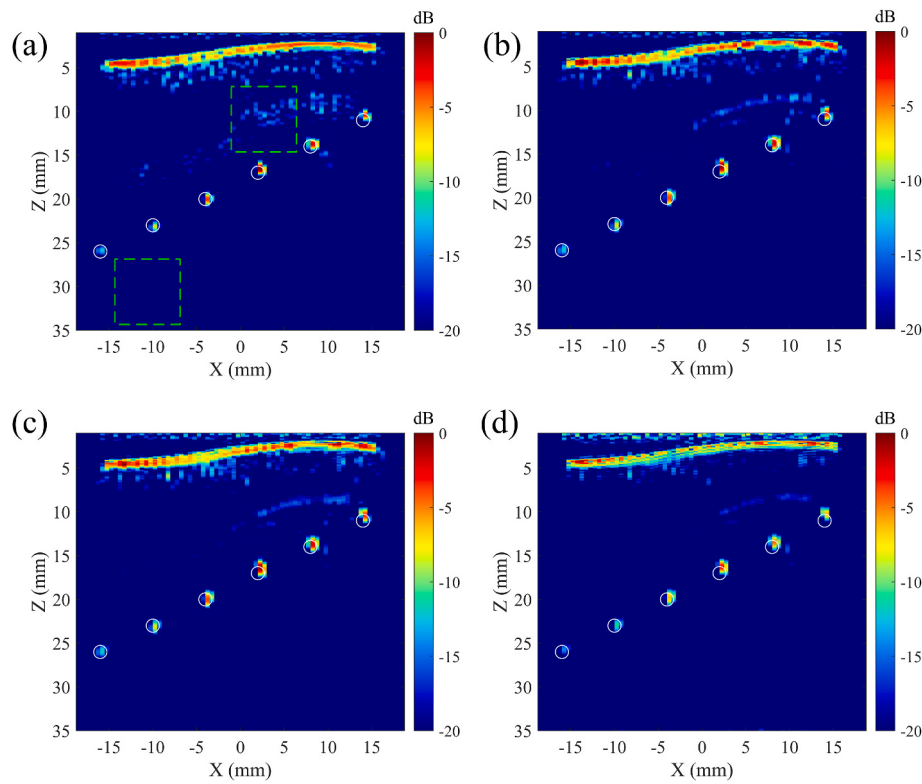


Fig. 7. Imaging results for (a) ENPSM, the green dotted area is the region of background noise for calculating SNR; (b) AA-ENPSM with $\tau = 4$, $\eta = 0.05$ mm; (c) AA-ENPSM with $\tau = 4$, $\eta = 0.10$ mm; (d) AA-ENPSM with $\tau = 4$, $\eta = 0.30$ mm, for the copper alloy sample. (For interpretation of the references to color in this figure legend, the reader is referred to the Web version of this article.)

calculating SNR in Fig. 7(a), and the background noise region is the same for each calculation of SNR in the different conditions. Average SNRs of all SDH for values of τ varying from 1 to 8 and η varying from 0.05 to 0.40 mm are generated for different pixel sizes of 0.2 mm*0.5 mm, 0.1 mm*0.5 mm, and 0.05 mm*0.5 mm as shown in Fig. 8. Regardless of the pixel size, the average SNR is seen to grow rapidly with the refined index τ before converging to a steady value. It is due to the fact that when there are enough sub-grids, the average weighting value Ω_2'' of the entire grid converges. In our case, $\tau = 4$ is sufficient because the geometric contour curve is quite smooth. Meanwhile, the optimal offset distance η considering different pixel sizes is ~ 0.10 mm in our case, allowing for the highest possible image quality. This optimum value is probably associated with the -14dB threshold used to define the leading edge. When the pixel size of 0.2 mm*0.5 mm, 0.1 mm*0.5 mm, and 0.05 mm*0.5 mm, the average SNR of the original ENPSM algorithm, whose is 16.3 dB, 19.5 dB, and 22.4 dB, respectively. It is clear that utilizing excessive offset in AA-ENPSM produces poorer image

quality than ENPSM. Therefore, 4 and 0.10 mm were chosen for τ and η in the following sections.

4.2. AC-ENPSM without anti-aliasing

It is well known that phased array imaging is significantly impacted by filtering. For instance, different SNRs are obtained by applying various filtering bandwidths. In this study, the frequency range of attenuation compensation is also influenced by the bandwidth selection, thus we begin with a discussion about the bandwidth. For a center frequency of 5 MHz, imaging results for the attenuation compensation ENPSM (AC-ENPSM) algorithm at bandwidths of 1–9, 2–8, 3–7, and 4–6 MHz are presented in Fig. 9(a–d) for the copper alloy sample and Fig. 9(e–h) for the aluminum alloy sample. Note that the size of pixel grid is set as 0.1 mm*0.5 mm in Fig. 9. To address the excessive compensation on the bottom of image and absence of diffraction correction, the attenuation compensation for the copper alloy sample is truncated at a

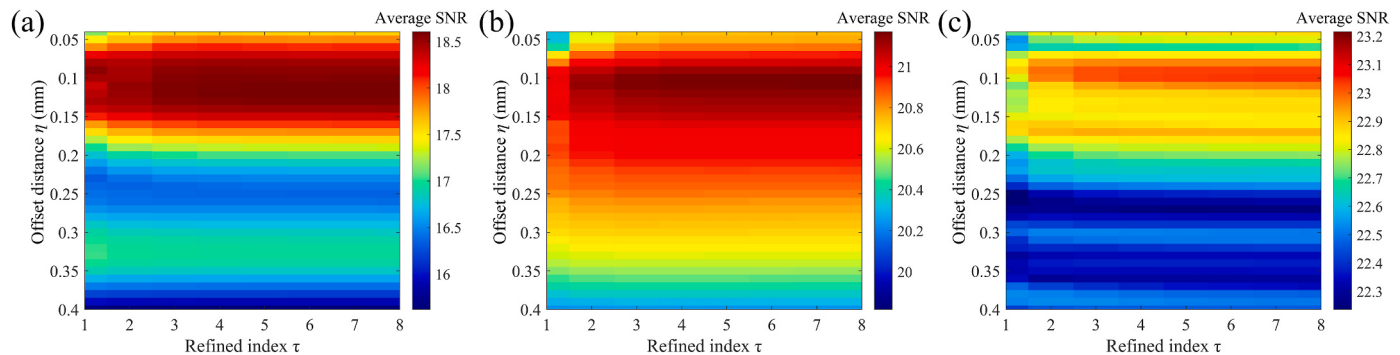


Fig. 8. Average SNRs of all SDH for the copper alloy sample for varying values of the refined index τ and offset distance η , for pixel grids of (a) 0.2 mm*0.5 mm; (b) 0.1 mm*0.5 mm; and (c) 0.05 mm*0.5 mm.

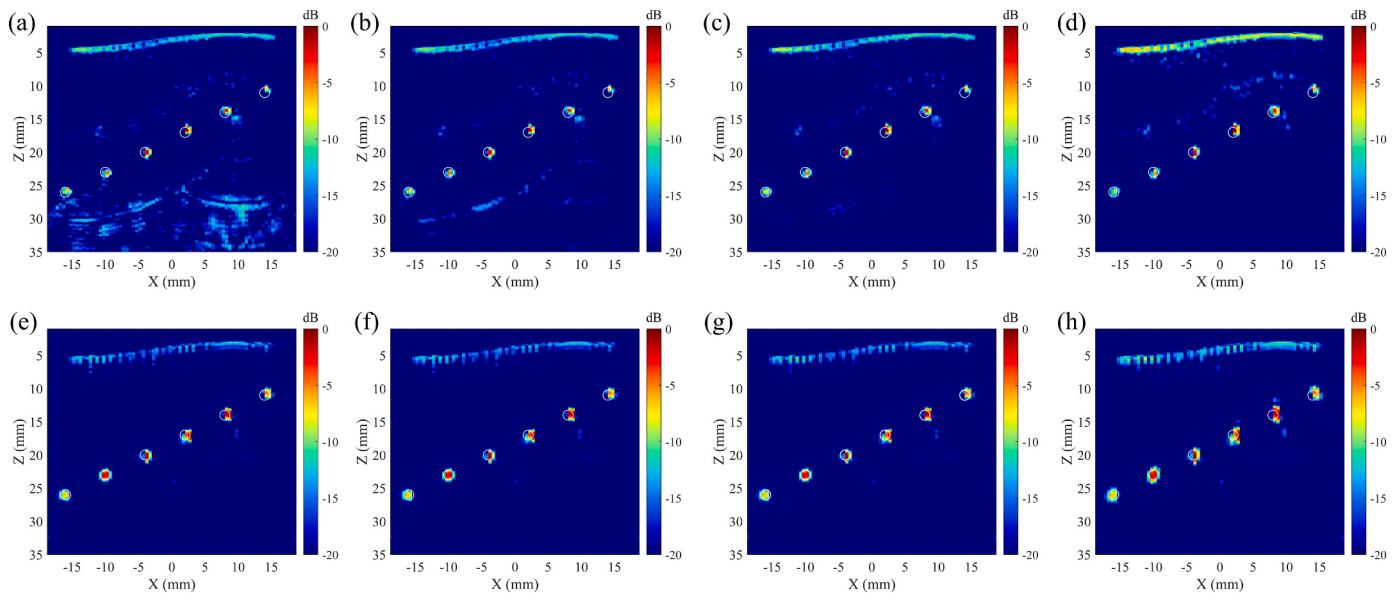


Fig. 9. Imaging results from AC-ENPSM for varying bandwidths: (a) 1–9 MHz; (b) 2–8 MHz, (c) 3–7 MHz, (d) 4–6 MHz for the copper alloy sample; (e) 1–9 MHz; (f) 2–8 MHz, (g) 3–7 MHz, (h) 4–6 MHz for the aluminum alloy sample.

depth of $z = 28$ mm and then maintained, while the attenuation compensation of the aluminum alloy sample is untruncated due to its weak attenuation.

From Fig. 9(a–c), we see that the AC-ENPSM results for the copper alloy sample show strong artifacts; however, when we narrow the bandwidth to 4–6 MHz for the copper alloy sample, there are fewer artifacts as shown in Fig. 9(c). One of the reasons might be that the higher frequency information is lost due to the strong attenuation and noise contamination. Unfortunately, limiting the bandwidth could lead to less detailed information on the defects, such as their shapes and sizes. Fig. 9(h) shows the negative effects of the cut-off frequency for the aluminum alloy sample. Distortion of defects is present, which may also pose problems in terms of comprehensively evaluating the quality and performance of the tested objects. In addition, the bandwidth selection has an impact on PSM imaging's computational efficiency. In short, there is a trade-off between defect distortion, SNR level, and computational efficiency.

To carry out an objective comparison of the imaging results at different bandwidths, the calculation times and average SNRs of all SDH are presented in Fig. 10. Note that Fig. 10(a) shows the mean and error bar of the calculation time based on ten runs. The calculation time decreases as the bandwidth is narrowed, and the attenuation compensation has very little effect on the time cost. From Fig. 10(b), we see that the average SNR decreases as the bandwidth becomes shorter for ENPSM, meaning that the loss of frequency information makes the imaging worse. However, for a material with high attenuation such as copper, it is evident that narrowing the bandwidth and employing the AC-ENPSM algorithm is beneficial. Furthermore, the application of attenuation compensation for the aluminum alloy sample with weak attenuation might be not necessary. It is likely to result in a lower average SNR due to superfluous compensation for the background noise. Combining the defect distortion depicted in Fig. 9 with the SNR and calculation time depicted in Fig. 10, a bandwidth of 4–6 MHz was selected for the copper alloy sample, and 3–7 MHz for the aluminum alloy sample.

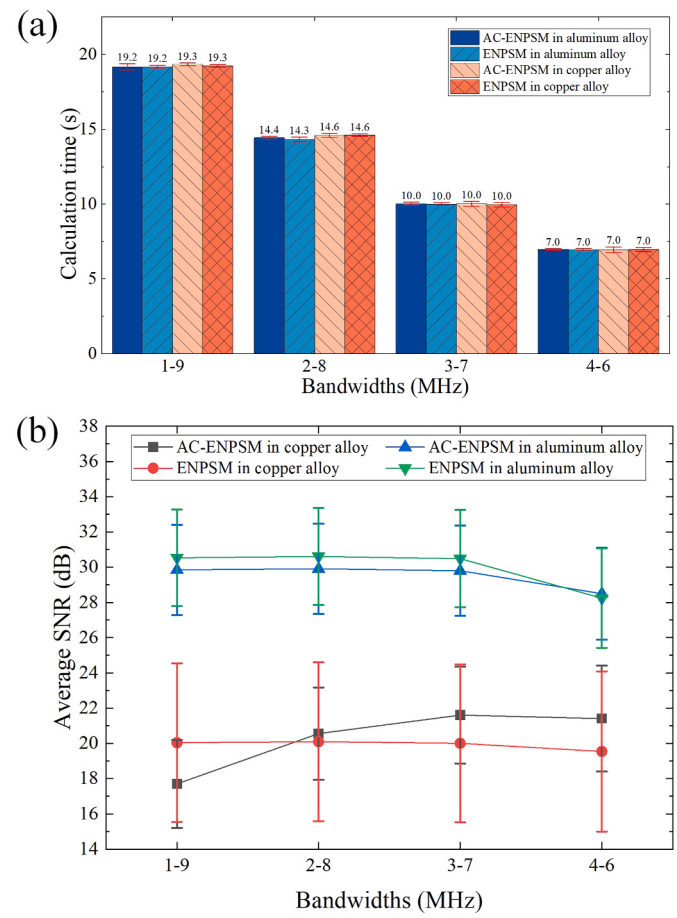


Fig. 10. Imaging performance for different bandwidths: (a) calculation time; (b) average SNR.

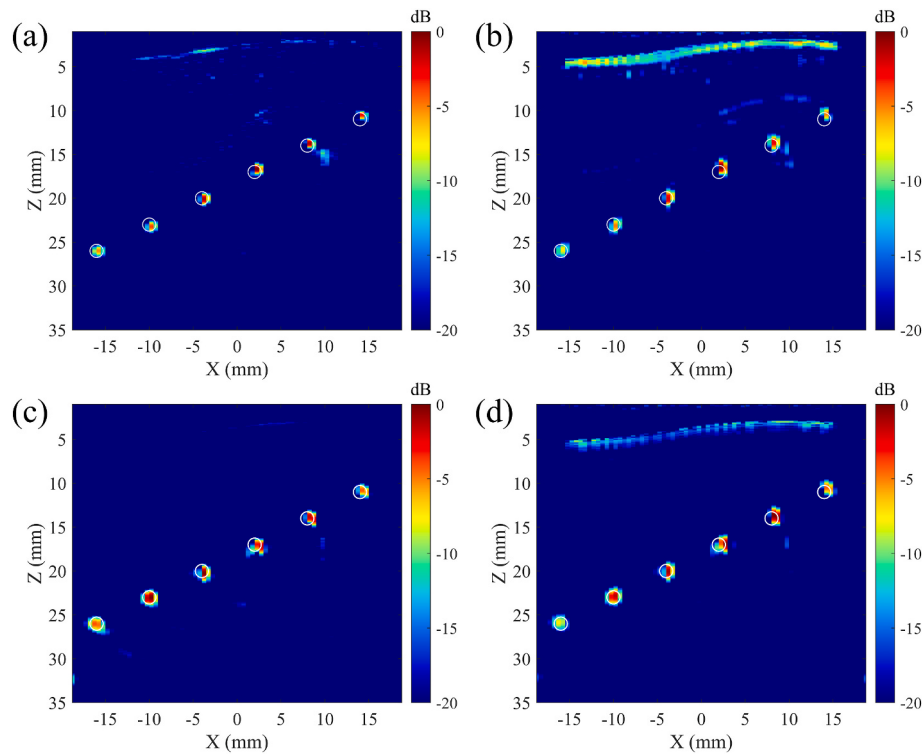


Fig. 11. Comparison of the results from (a) ray-based TFM, (b) AC-AA-ENPSM for the copper alloy sample; (c) ray-based TFM, and (d) AC-AA-ENPSM for the aluminum alloy sample.

4.3. Comparison between ENPSM-based methods and ray-based TFM

In Sections 4.1 and 4.2, we discussed the imaging performance for the anti-aliasing technique and attenuation compensation steps. Optimal values of the offset distance, refined index, and bandwidth parameters were obtained. Imaging results from a combination of attenuation compensation, anti-aliasing, and ENPSM are presented in Fig. 11(b,d). The TFM algorithm is used as a reference for comparison of the imaging results from AC-AA-ENPSM, as it is widely used in ultrasonic imaging of NDT; it is precalculated using Snell's ray-tracing process [25–28] to get the delay-law in terms of irregular surface components. Although the ray-based TFM algorithm used in this section is the basic one, whose calculation time can be greatly reduced by GPU acceleration or some appropriate procedures, such as changing the iterative mathematical approach [29] and calculating the propagation time approximately [30], those improvements may degrade the display at the cost of iteration quality or time accuracy. To ensure the best display result, therefore, those enhancements are not used, and we believe that the imaging experiment performed without the use of the GPU is acceptable. The imaging results from ray-based TFM are presented in Fig. 11(a,c). The size of pixel grid is set as 0.1 mm*0.5 mm in both the ray-based TFM and AC-AA-ENPSM imaging results.

Although the ray-based TFM algorithm still gives a strong artifact near SHD #2, this method clearly shows the SDHs in the copper alloy sample. It indicates that the delay-and-sum technique has significant advantages in off-line post-processing analysis. For the aluminum alloy sample shown in Fig. 11(c and d), the AC-AA-ENPSM algorithm produces a superior result than the ray-based TFM approach, with a greater SNR and a more integrated surface contour. The display of the surface contour plays an important role in locating internal defects in the sample.

As shown in Fig. 12, the SNR of the individual SDHs is used to evaluate the performance of the different methods. For the copper alloy sample, AC-AA-ENPSM achieves the best performance of the ENPSM-based methods; there is a huge improvement compared with ENPSM,

especially for deep SDHs such as #5 and #6. The AC-AA-ENPSM has an average SNR that is just 1.9 dB lower than the ray-based TFM, while the SNR is incapable of assessing the integrity of the surface contour. Most importantly, the AC-AA-ENPSM is substantially faster than the ray-based TFM in the CPU-only environment, and the calculation times for ENPSM-based methods will be further reduced as a benefit of the use of GPU and the frequency cut-off. For aluminum alloys, the SNR values of AA-ENPSM for #1 to #4 are higher than AC-AA-ENPSM, and its average SNR is 0.4 dB higher. It can be seen that the anti-aliasing technique yields a better effect than attenuation compensation in terms of the imaging results for the aluminum alloy sample. Moreover, the AA-ENPSM not only has an average SNR of 2.3 dB greater than the ray-based TFM, but also is 41.7 times more computationally efficient. It should be noted that the attenuation compensation and anti-aliasing steps were found to have almost no effect on the time cost.

To determine the quantification accuracy of the defects, an analysis of the individual defects was carried out using the -6 dB contour of the defect boundary. A linear interpolation of the pixel amplitude was used to determine the SDH profile and the -6 dB area was then calculated. The areas of the SDH defects for the copper alloy and aluminum alloy samples are shown in Table 1.

Since the diameter of all SDH defects was 1.5 mm, the value of the correct area is 1.7671 mm². All of the values in Table 1 are lower than the correct value. Using the average SDH areas of the images as a measure of the performance of the different methods, we see that AC-AA-ENPSM achieves the closest results to the correct defect area for the copper alloy sample with an average defect area of 0.9100 mm², and for the aluminum alloy sample with an average defect area of 1.2476 mm². The errors in the calculated image defect areas are -48.51% and -29.40% for the copper and aluminum alloys; thus, the errors in equivalent diameters are -28.24% and -15.98%, respectively. The performance of AC-AA-ENPSM in terms of identifying the sizes of SDH defects is better than for ray-based TFM.

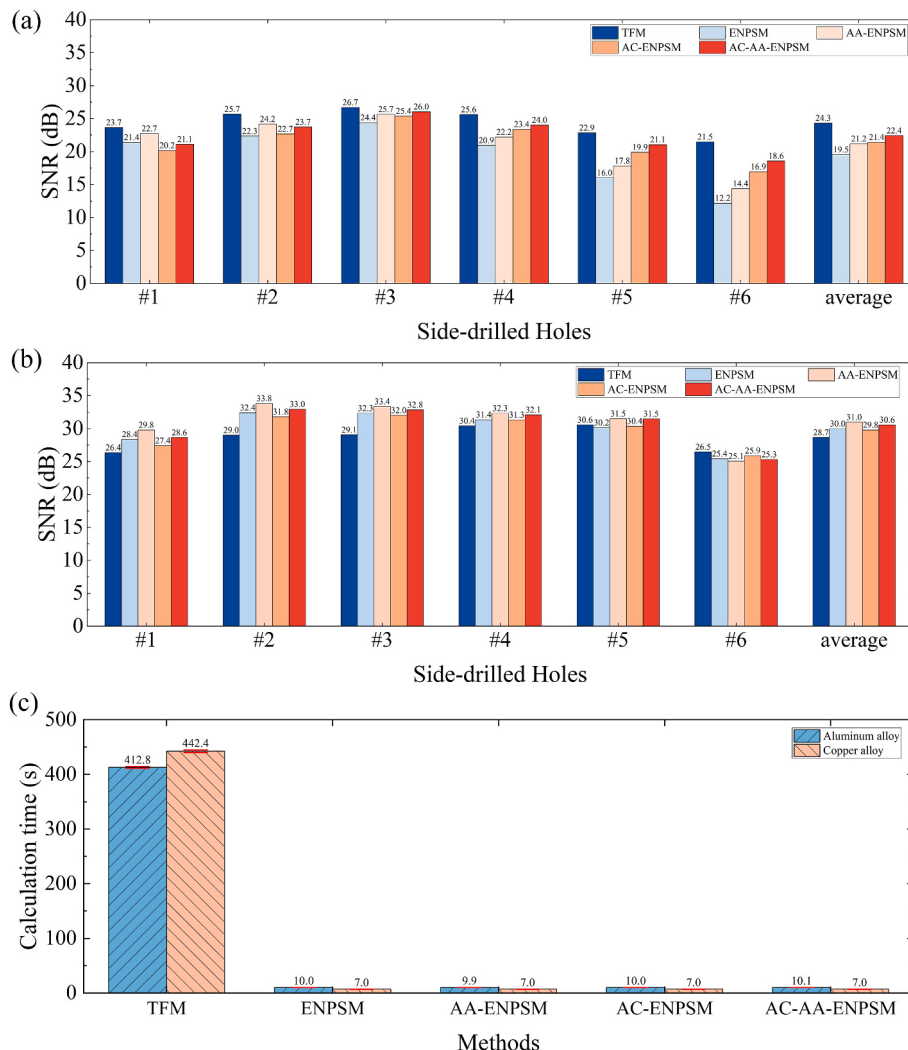


Fig. 12. Imaging performance for different methods: (a) SNRs for the copper alloy sample; (b) SNRs for the aluminum alloy sample; (c) calculation times.

Table 1

Results for the -6 dB area of SDHs (mm^2).

No.	-6 dB area for the aluminum alloy		-6 dB area for the copper alloy	
	Ray-based TFM	AC-AA-ENPSM	Ray-based TFM	AC-AA-ENPSM
#1	0.9921	1.2143	0.4103	0.6949
#2	1.0250	1.2298	0.4159	0.8756
#3	1.0518	0.9197	0.5158	0.8014
#4	0.7263	0.8908	0.5616	0.8875
#5	1.2287	1.3925	0.6270	0.9344
#6	1.7154	1.8382	0.8414	1.2660
Average	1.1232	1.2476	0.5620	0.9100
Error	36.44%	29.40%	68.20%	48.51%

5. Conclusion

We have presented an improved algorithm called AC-AA-ENPSM for processing ultrasonic data from irregular surface components, which includes attenuation compensating and anti-aliasing. To compare and analyze the imaging results from the ENPSM, AA-ENPSM, AC-ENPSM, AC-AA-ENPSM, and ray-based TFM algorithms, aluminum alloy and copper alloy samples with SDH defects and irregular surfaces were used as experimental objects. The proposed ENPSM-based algorithms can improve the display of SDH defects inside irregular surface components. Compared with ray-based TFM, the AC-AA-ENPSM method achieved a

more integrated profile, lower errors in the sizes of the SDHs, and a lower computational burden. With suitable bandwidth and anti-aliasing parameters, this method could be used for high-quality imaging in NDT. For industrial applications such as real-time imaging of complex objects, parallel processing and GPU acceleration for the proposed method is in progress. With attenuation measurement on samples of non-parallel top and bottom surfaces proposed [31,32], a cross-method is needed to improve the imaging efficiency in practice. In future, diffusion compensation could also be taken into consideration in addition to attenuation compensation. The automatic categorization of multiple front wall echoes and the first front wall echoes of other layer interfaces should be noted as well.

Author statement

Juncen Wu: Methodology, Software, Formal analysis, Writing - Original Draft, Validation, Visualization, Investigation. **Hongwei Hu:** Resources, Supervision, Funding acquisition, Writing - Review & Editing, Supervision, Project administration. **Yongfeng Song:** Conceptualization, Validation, Formal analysis, Writing - Original Draft, Writing - Review & Editing, Supervision, Investigation. **Duo Lyu:** Supervision. **Xiongbing Li:** Resources.

Declaration of competing interest

The authors declare that they have no known competing financial interests or personal relationships that could have appeared to influence the work reported in this paper.

Data availability

Data will be made available on request.

Acknowledgements

This work was supported by the National Natural Science Foundation of China (Grant No. 52075049), the Natural Science Foundation of Hunan Province (Grant No. 2020JJ2028), Hunan Provincial Key Research and Development Program (Grant No. 2022GK2058), and Changsha City Planned Science and Technology Project (Grant No. kq2014100).

References

- [1] Barkefors Tomhsa. Ultrasonic imaging of immersed objects using migration techniques conf synthetic aperture radar. European 2010;442–5.
- [2] Gazdag J. Wave equation migration with phase-shift method. Geophysics 1978;43: 1342–51.
- [3] Jensen JA, Nikolov SI, Gammelmark KL, Pedersen MH. Synthetic aperture ultrasound imaging. Ultrasonics 2006;44:e5–15.
- [4] Olofsson T. Phase shift migration for imaging layered objects and objects immersed in water. IEEE Trans Ultrason Ferroelectrics Freq Control 2010;57:2522–30.
- [5] Skjelvareid MH, Olofsson T, Birkeland Y, Larsen Y. Synthetic aperture focusing of ultrasonic data from multilayered media using an omega-K algorithm. IEEE Trans Ultrason Ferroelectrics Freq Control 2011;58:1037–48.
- [6] Qin K, Yang C, Sun F. Generalized frequency-domain synthetic aperture focusing technique for ultrasonic imaging of irregularly layered objects. IEEE Trans Ultrason Ferroelectrics Freq Control 2014;61:133–46.
- [7] Lukomski T. Non-stationary phase shift migration for flaw detection in objects with lateral velocity variations. Insight - Non-Destruct. Test. Condition Monit. 2014;56: 477–82.
- [8] Mao Q, Chen Y, Chen M, Shi W, Lu C, Li Q. A fast interface reconstruction method for frequency-domain synthetic aperture focusing technique imaging of two-layered systems with non-planar interface based on virtual points measuring. J Nondestr Eval 2020;39:41.
- [9] Wu H, Chen J, Yang K, Hu X. Ultrasonic array imaging of multilayer structures using full matrix capture and extended phase shift migration. Meas Sci Technol 2016;27:045401.
- [10] Lukomski T. Full-matrix capture with phased shift migration for flaw detection in layered objects with complex geometry. Ultrasonics 2016;70:241–7.
- [11] Chang J, Chen Z, Luo W, Zhong H, Lu C. Extended non-stationary phase-shift migration for ultrasonic imaging of irregular surface component. IEEE Access 2021;9:3004–15.
- [12] Ji K, Zhao P, Zhuo C, Chen M, Chen J, Jin H, et al. Ultrasonic autofocus imaging of internal voids in multilayer polymer composite structures. Ultrasonics 2022;120: 106657.
- [13] Jiang C, Li Y, Xu K, Ta D. Full-matrix phase shift migration method for transcranial ultrasonic imaging. IEEE Trans Ultrason Ferroelectrics Freq Control 2021;68: 72–83.
- [14] Jin H, Zheng Z, Liao X, Zheng Y. Image reconstruction of immersed ultrasonic testing for strongly attenuative materials. Mech Syst Signal Process 2022;168: 108654.
- [15] Margetan FJ, Gigliotti M, Brashe L, Leach W. Fundamental studies: inspection properties for engine titanium alloys. 2002.
- [16] Yu L, Margetan FJ, Thompson RB, Degtyar A. Survey of ultrasonic properties of aircraft Engine Titanium forgings. AIP Conf Proc 2002;615:1510–7.
- [17] Lukomski T, Stepinski T. Imaging multilayered objects with complex geometry. In: 19th world conference on non-destructive testing. Munich, Germany: Curran Associates, Inc; June; 2016. p. 1214–25.
- [18] Schmerr L. Fundamentals of ultrasonic nondestructive evaluation: a modeling approach. second ed. New York: Springer; 2016.
- [19] Schleicher J, Costa JC, Novais A. A comparison of imaging conditions for wave-equation shot-profile migration. Geophysics 2008;73:S219–27.
- [20] Kelly JF, McGough RJ, Meerschaert MM. Analytical time-domain Green's functions for power-law media. J Acoust Soc Am 2008;124:2861–72.
- [21] Margetan FJ, Thompson RB, Yalda-Mooshabadi I, Han YHK. Detectability of small flaws in advanced engine alloys. 1993.
- [22] Song Y, Turner JA, Peng Z, Chen C, Li X. Enhanced ultrasonic flaw detection using an ultrahigh gain and time-dependent threshold. IEEE Trans Ultrason Ferroelectrics Freq Control 2018;65:1214–25.
- [23] Moles M. Ultrasonic phased array. NDT Tech. 2012;11:1–5.
- [24] Zhuang Z, Zhang J, Lian G, Drinkwater BW. Comparison of time domain and frequency-wavenumber domain ultrasonic array imaging algorithms for non-destructive evaluation. Sensors 2020;20:4951.
- [25] Hunter AJ, Drinkwater BW, Wilcox PD. Autofocusing ultrasonic imagery for non-destructive testing and evaluation of specimens with complicated geometries. NDT E Int 2010;43:78–85.
- [26] Sutcliffe M, Weston M, Charlton P, Donne K, Wright B, Cooper I. Full matrix capture with time-efficient auto-focusing of unknown geometry through dual-layered media. Insight - Non-Destruct. Test. Condition Monit. 2013;55:297–301.
- [27] Hu H, Du J, Li Y, Zhou Z. Two-layer medium ultrasonic phased array total focusing method imaging based on sparse matrix. J Mech Eng 2017;53:128–35.
- [28] Hu H, Du J, Xu N, Jeong H, Wang X. Ultrasonic sparse-TFM imaging for a two-layer medium using genetic algorithm optimization and effective aperture correction. NDT E Int 2017;90:24–32.
- [29] Mineo C, Cerniglia D, Mohseni E. Solving ultrasonic ray tracing in parts with multiple material layers through Root-Finding methods. Ultrasonics 2022;124: 106747.
- [30] Zhang J, Drinkwater BW, Wilcox PD. Efficient immersion imaging of components with nonplanar surfaces. IEEE Trans Ultrason Ferroelectrics Freq Control 2014;61: 1284–95.
- [31] Truell R, Oates W. Effect of lack of parallelism of sample faces on the measurement of ultrasonic attenuation. J Acoust Soc Am 1963;35:1382–6.
- [32] Lobkis OI, Rokhlin SI. Measurement of attenuation in a sample with nonparallel surfaces. Ultrasonics 2022;124:106760.